ACS Photonics

pubs.acs.org/journal/apchd5

Article

A $LiNbO_3$ Platform with Tailored Thickness Bridging Bulk and Thin Film: Application to Broadband Frequency Conversion

Aiman Zinaoui, Martin Khouri, Jean-David Fayssaud, Arthur De Sousa Lopes Moreira, Miguel Angel Suarez, Samuel Queste, Laurent Robert, Ludovic Gauthier-Manuel, Mathieu Chauvet, and Nadège Courjal*

Cite This: https://doi.org/10.1021/acsphotonics.5c01334 Read Online

ACCESS | Metrics & More | Article Recommendations | Supporting Information

ABSTRACT: We introduce a monolithic $LiNbO_3$ membrane platform that bridges bulk and thin-film approaches, enabling custom-tailored waveguide cross sections. Using a combination of saw dicing and reactive ion etching (RIE), we fabricate $LiNbO_3$ structures with adaptable thicknesses ranging from 400 nm to several microns, identifying 2 μm as an optimal value for addressing key challenges in frequency conversion. Our platform demonstrates robust second harmonic generation (SHG) with a broad pump wavelength response of up to 150 nm within the C-band at room temperature, achieved by tuning the waveguide thickness, while maintaining low coupling losses of 0.8 dB/facet. These results represent a significant step toward versatile integrated photonic systems, advancing applications in broadband spectroscopy, quantum information processing, and sensing through efficient and spectrally agile nonlinear frequency conversion.

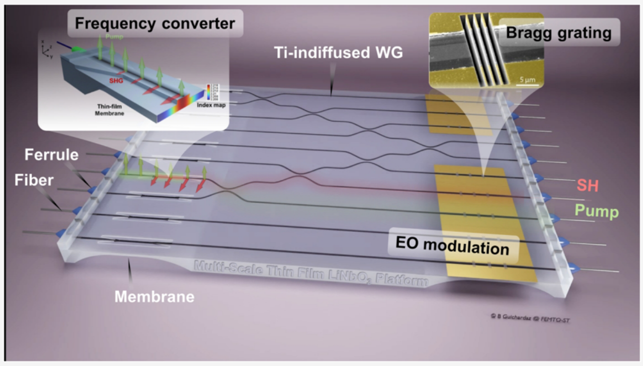

KEYWORDS: *thin-film lithium niobate, nonlinear optics, second-harmonic generation, integrated photonics, electro-optic devices, broadband frequency conversion*

INTRODUCTION

Lithium niobate ($LiNbO_3$) is a cornerstone material in integrated photonics, valued for its strong second-order nonlinearity, reproducible fabrication, low propagation losses, and wide transparency range. Since the commercial introduction of submicrometer thin-film lithium niobate (TFLN) in 2010, the technology has advanced significantly, positioning $LiNbO_3$ at a pivotal stage between traditional weakly confined platforms and TFLN-based integrated photonics. Conventional waveguiding techniques, such as titanium indiffusion and proton exchange, have long underpinned $LiNbO_3$ photonic systems. Their weak optical confinement facilitates efficient fiber coupling and robust packaging, making them well-suited for high-bit-rate telecommunications and loss-sensitive quantum optics applications.[1]

However, the increasing demand for compact, high-performance photonic circuits has driven a transition toward TFLN platforms, which enable submicron optical confinement, leading to higher integration densities and advanced functionalities in photonics and quantum circuits.[2,3] Moreover, TFLN offers strong potential for frequency conversion applications due to its reduced cross-section enabling high nonlinear conversion efficiency, especially in periodically poled lithium niobate (PPLN) structures.[4−6] But the thin film implementation of PPLN also poses challenges. The reduced waveguide cross-section increases sensitivity to fabrication fluctuations, making it difficult to precisely control the operating wavelength and to maintain phase matching over more than a few millimeters. To address this issue, mitigation strategies such as patterning multiple waveguides per poling period,[7] trimming,[8] or adapting the poling process after waveguide fabrication[9] are required, adding cost or complexity and potentially leading to yield losses.

Beyond fabrication tolerances, large-scale adoption of TFLN faces global wafer production limitations and consequently higher costs than standard technologies. Optical coupling in TFLN circuits remains another challenge, often requiring specialized fiber interfaces, including tapered,[10] lensed,[11] or high numerical aperture fibers,[12] as well as multilayer taper or 3D coupling schemes.[12]

An intermediate solution involves micrometric-thick $LiNbO_3$ film achieved through wafer thinning, which strike a

Received: June 10, 2025
Revised: August 18, 2025
Accepted: August 19, 2025

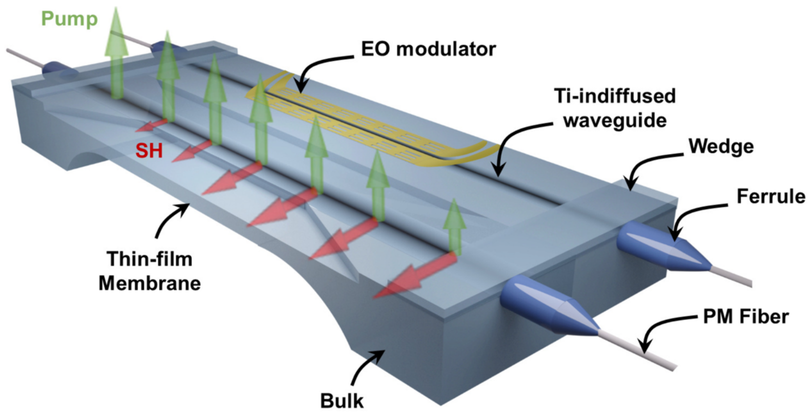

Figure 1. Artistic view of a $LiNbO_3$ chip with suspended membranes. This platform is suitable for a wide range of applications, including EO modulators, photonic crystals, and nonlinear devices. The structure shown at the back of the figure corresponds to an EO modulator, previously demonstrated in ref 16, exhibiting a tunability of 60 pm/V. In the foreground, we present a nonlinear waveguide designed for broadband and highly tunable SHG.

balance between competitive light confinement and fiber compatibility. These platforms also offer relaxed fabrication tolerances[13] while offering improved resistance to high-power light. For instance, SHG waveguides with cross-sectional areas of 3 × 4 μm^2 demonstrate a SHG conversion efficiency of 1320%/W with an insertion loss of 3.8 dB.[14] Micrometer-thick $LiNbO_3$ films also open the way to birefringence phase matching, avoiding periodic poling PPLN and offering high-temperature tuning capability.[15] However, a micrometer-thick waveguide on SiO_2 is multimode, which can hinder data processing or induce higher losses in curved patterns, unless cautious is taken to excite mainly the fundamental mode of the structure. Moreover, the process of wafer thinning introduces a significant challenge to reach an adequate total thickness variation (TTV) of the guiding layer across the wafer. While postprocessing trimming can improve this accuracy to within 10 nm, the required equipment remains difficult to access, presenting a barrier to widespread implementation.

To address these limitations, a monolithic multiscale platform that combines bulk and thin-film approaches, enabling any thickness ranges (Bulk, micrometer-thick, and submicrometer thick) on a single wafer with accessible technologies, can offer significant advantages, including simplified fiber coupling, high power handling, and precise local confinement control. Our previous work[16−18] demonstrated early progress toward this goal by developing a precision circular saw dicing technique to locally thin Ti-indiffused waveguides. This method forms thinned regions hosting micromodulators with 60 pm/V electro-optic tuning efficiency[16] or SHG via birefringence phase matching, with a broad 150 nm emission bandwidth and 10 nm/°C temperature tunability.[18] Additionally, the circular saw naturally forms an adiabatic taper during thinning, ensuring a smooth transition from the thinned zone to weakly confined Ti-indiffused waveguides. This built-in tapering facilitates fiber coupling, achieving a coupling loss of 0.8 dB per facet with standard SMF28 fibers.[17] However, the blade vertical positioning inaccuracy (≈1 μm) is a challenge necessitating mitigation strategies to determine the right operating point and restricting widespread adoption.

In this work, we introduce a method combining RIE with noninvasive tomography diagnostics, enabling the fabrication of $LiNbO_3$ membranes with thicknesses ranging from 400 nm to tens of microns with 20 nm precision. A key advantage of our approach is its ability to fine-tune membrane thickness after fabrication, offering flexibility across a wide range of TFLN and micrometric platforms. This method enables on-demand adjustment of operational parameters in devices such as photonic crystals, modulators, and frequency converters.

We showcase thereby a SHG device with a 150 nm bandwidth in the C-band via type-I phase matching at ambient temperature. This achievement opens new possibilities for broadband spectrometers and wavelength-division multiplexers. Our approach relaxes the strict subnanometer fabrication tolerances typically required for broadband TFLN-based PPLN architectures.[7] It offers a competitive nonlinear conversion efficiency of 35%/W/cm^2 and robust performance at CW optical power up to 500 mW. This combination of broadband operation, ambient temperature functionality, and fabrication simplicity positions our platform as a practical and flexible solution for advanced photonic applications.

RESULTS AND DISCUSSION

Design, Fabrication, and Precision Calibration. Figure 1 presents an artistic illustration of the proposed monolithic $LiNbO_3$ platform. The device features Ti-indiffused waveguides, which are laterally etched to form rib waveguides. Local thinning is then performed using precision circular saw dicing, resulting in suspended TFLN regions with controllable thicknesses ranging from 400 nm to several tens of microns. The circular blade geometry enables smooth, low-loss transitions between the weakly confined input waveguides and the high-confinement TFLN region, without requiring additional lithography or structuring steps.

This approach enables the fabrication of a suspended micrometer-thick rib waveguide supporting SHG via type-I birefringent phase matching at ambient temperature. In the following, we detail the methodology developed to achieve accurate control of the TFLN thickness.

Fabrication Process. The fabrication process begins with the creation of titanium-diffused waveguides on a 500 μm-thick $LiNbO_3$ substrate. Additional steps, such as electrode deposition for EO modulators or rib waveguide etching for dispersion engineering, can be achieved afterward, targeting specific applications before proceeding with membrane

https://doi.org/10.1021/acsphotonics.5c01334
ACS Photonics XXXX, XXX, XXX−XXX

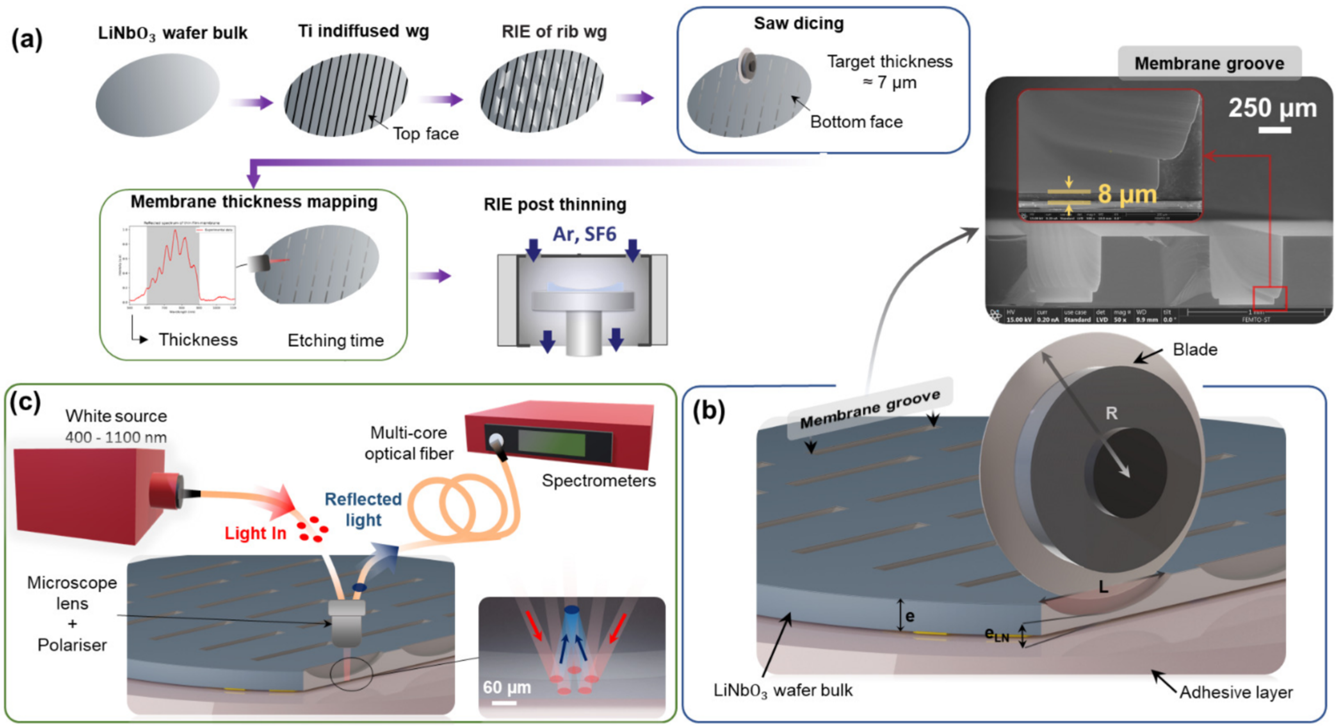

Figure 2. (a) Overview of the technological steps dedicated to membrane manufacturing. (b) Schematic view showing the key parameters required for local thinning of waveguides using a precision saw, along with an SEM image of the chip backside showing two suspended membranes separated by 1 mm. The red-boxed inset provides a zoomed-in view of the thinned cavity, highlighting the e_{LN} = 8 μm membrane thickness achieved after the two dicing steps. e is the initial thickness of the wafer, measured in a first calibration step. L is the blade footprint. The red-box inset also shows two groove widths, typical of a two-step process. (c) The experimental setup for nondestructive membrane thickness measurement.

thinning (as illustrated in the third step of Figure 2(a)). A suspended membrane is then formed by thinning the backside of the wafer down to a few micrometers. This step uses a precision sawing process with a Disco Dicing Saw 3350, followed by post-thinning correction using RIE to fine-tune the membrane thickness.

Scalable fabrication of long and thin $LiNbO_3$ membranes for wafer-level photonic integration requires overcoming the intrinsic limitations of conventional dicing techniques, most notably blade wear and positioning accuracy. While the saw blade method reported in ref 16 allows localized membrane formation, it is unsuitable for wafer-scale integration or fabricating membranes longer than 3 mm. Blade degradation leads to inconsistent cutting depth, frequent releveling is required to maintain precision and membrane integrity.

To address these issues, we developed a new dicing process. It relies on bonding the patterned face of the wafer onto a blank $LiNbO_3$ support wafer using NOA 1382 optical adhesive. Its low viscosity (15−25 cps) ensures uniform bonding, while the support wafer provides mechanical stability during dicing and structural consolidation after processing. Thinning is then carried out in two steps: an initial cut using a wear-resistant metallic blade, followed by a polishing blade that smooths the groove and reduces the membrane to a target thickness of 8 μm. The details of this cutting method are provided in the Methods section.

However, many photonic applications, particularly those involving nonlinear interactions, require micrometric or submicrometric thicknesses to enhance light confinement and phase-matching conditions. To reach such thin dimensions with high precision, we developed a postprocessing thinning technique based on RIE, capable of reducing the membrane thickness down to the submicron scale with high precision.

This process combines both chemical and physical etching mechanisms and is conducted in controlled steps of 30 min etching intervals, each followed by a 10 min resting period. These pauses allow for thermal stabilization, which helps prevent membrane damage, ensures plasma stability, and maintains uniform etching rates. During processing, the sample is maintained at 20 °C with the membrane cavity side facing the plasma ion flux, ensuring uniform etching across the surface.

To accurately predict the etching duration required to reach a target thickness e_{LN}, we constructed an empirical model describing the evolution of the membrane thickness as a function of etching time:

$$e_{LN} = (e_{LN_0} + C)\cdot\exp(-k\cdot\text{time}) - C \qquad (1)$$

Where e_{LN_0} is the initial thickness after the dicing step, k is the decay factor primarily influenced by the etching rate equal to 1.52×10^{-3} min^{-1}, and C is a correction factor equal to 2.71 μm for submicron thicknesses. This model, derived from experimental data collected across multiple membranes and etching durations, offers a reliable way to predict the etching time required to reach a desired final thickness. Additional details regarding the construction of this model are presented in the Methods section.

Accordingly, eq 1 provides an estimation of the etching time required to thin membranes with initial thickness e_{LN_0}. To determine e_{LN_0}, we developed a nondestructive method (shown in Figure 2(c)) based on white light reflectometry of a beam focused to a 40 μm (detailed in the Supporting Information).

https://doi.org/10.1021/acsphotonics.5c01334
ACS Photonics XXXX, XXX, XXX−XXX

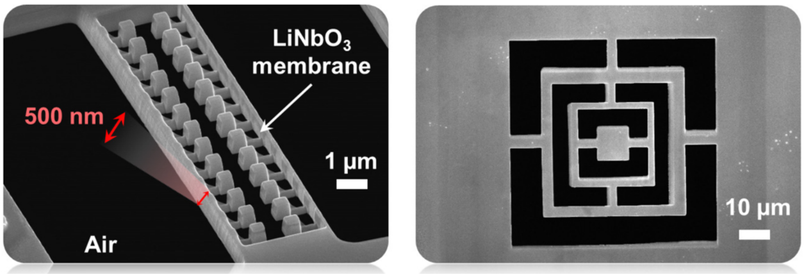

Figure 3. SEM images of a submicrometric thick membrane made by precise dicing and subsequently structured by FIB milling.

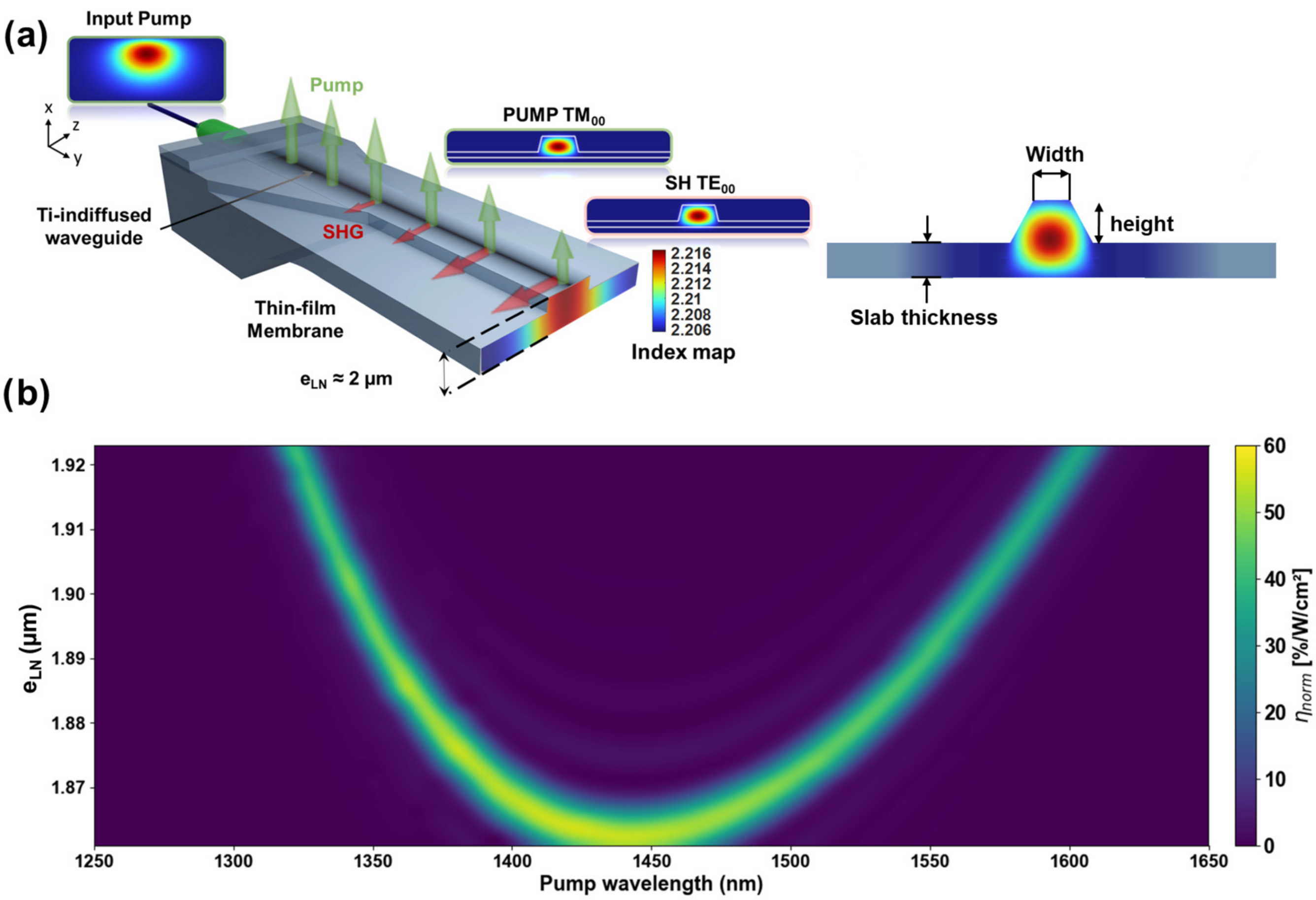

Figure 4. (a) Schematic illustration showing the optical modes and the adiabatic transition from the input Ti-indiffused waveguide to the nonlinear section where SHG occurs, along with a depiction of the rib waveguide structure and the geometrical parameters that control its dispersion. (b) Calculated phase-matching wavelength versus waveguide thickness e_{LN}.

The membrane thickness is measured after successive RIE etching cycles, which ensures a thickness control with an accuracy of 20 nm.

Figure 3 presents SEM images of submicron membranes fabricated using the above-described technique. These membranes were subsequently structured using FIB milling to demonstrate a variety of pattern geometries.

To illustrate the potential of the $LiNbO_3$ membranes, the following section details the fabrication of a SHG component based on the previously described technique. This component holds significant promise for applications such as ultrawide nonlinear frequency conversion.

Application: Nonlinear Frequency Conversion Device. Expanding the capabilities of frequency converters in thin-film $LiNbO_3$ waveguides requires an optimized design that maximizes the interaction length while ensuring a broad response bandwidth. This is particularly crucial for applications demanding broadband operation in the mid-infrared (MIR) or visible range.[19,20]

Conventional frequency conversion devices based on type-0 quasi-phase-matching (QPM) through periodically poled $LiNbO_3$ (PPLN) are often constrained by a narrow bandwidth in the telecom domain,[4] typically around 10 nm. While some studies have demonstrated broader responses in the MIR through tailored dispersion engineering and the $\chi^{(2)}$ interaction, achieving conditions where both group velocity mismatch (GVM) and group velocity dispersion (GVD) are minimized.[21] Such solutions remain scarce in the telecom range, where achieving broadband frequency conversion without sacrificing efficiency remains challenging.[22]

https://doi.org/10.1021/acsphotonics.5c01334
ACS Photonics XXXX, XXX, XXX−XXX

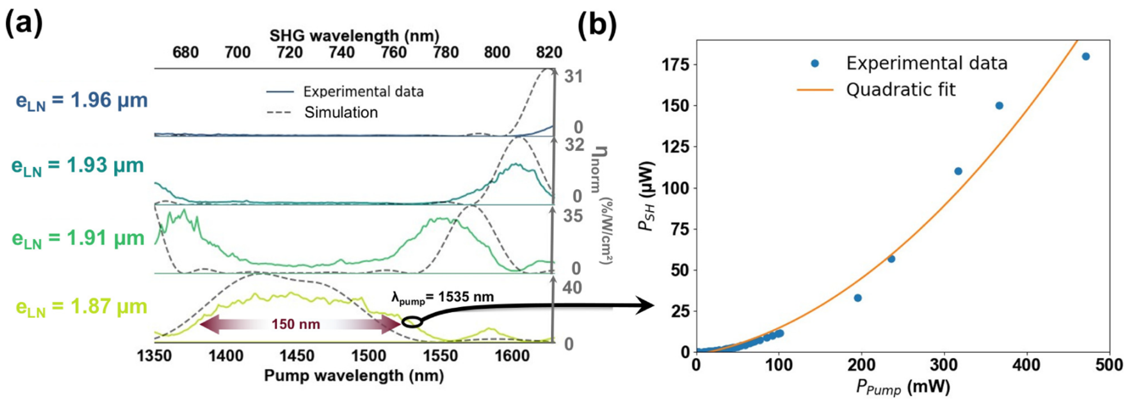

Figure 5. (a) Measured conversion efficiency as a function of rib waveguide thickness. (b) SH power as a function of pump power at 1535 nm, demonstrating the quadratic increase in SH signal power.

In our previous study,[18] we demonstrated a device combining perfect birefringent phase matching with a zero-GVM condition between the pump and second harmonic, significantly extending the conversion bandwidth to 150 nm-wide in the telecom C-band, leading to efficient conversion into a 75 nm-wide band in the visible range, with a conversion efficiency of 40%/W/cm^2. However, this device was leaning on the use of temperature to precisely set the phase matching condition, which can be a limiting factor for practical implementation.

To address this limitation, we propose a membrane-based rib waveguide that leverages type-I birefringence phase matching and dispersion engineering to achieve broadband frequency conversion at a chosen temperature, here at room temperature. This approach requires precise control of the thin-film thickness around 2 μm, where both phase matching and GVM vanish.

The device, illustrated in Figure 4(a), consists of a titanium-diffused input waveguide ensuring efficient coupling with SMF fibers.[17] Optical mode transition is facilitated by two tapers: a horizontal taper formed by etching and a vertical taper shaped by precision sawing, allowing a seamless transformation from a 30 μm^2 cross-section mode to a 5 μm^2 cross-section while minimizing propagation and transition losses. This architecture enables efficient light confinement in the suspended membrane region, where nonlinear interactions take place. This nonlinear region contains a rib waveguide, with its cross-section determined by parameters such as the etched height, width, and slab thickness, as shown in Figure 4(a).

In this structure, the fundamental pump mode (TM00) is polarized along the ordinary axis of $LiNbO_3$ (n_o), while the second harmonic (SH) is generated in the TE00 mode polarized along the extraordinary axis (n_e) when the phase-matching condition is fulfilled

$$\Delta k_o = \frac{4\pi}{\lambda_{pump}}(n_{SH} - n_{pump}) = 0 \tag{2}$$

Where n_{pump} and n_{SH} are the effective indices of the pump and SH modes, respectively. The phase-matching condition is governed by both the waveguide cross-section and the intrinsic birefringence of $LiNbO_3$. In this study, the refractive indices are deduced from Sellmeier's eqs[23,24] The waveguide cross-section is a key element for controlling the phase-matching wavelength. For instance, a waveguide cross-section of 23 μm^2 allows phase matching at two distinct wavelengths, one in the near-infrared (NIR) and the other in the mid-infrared (MIR). These two-phase matched wavelengths merge to give a broadband response in the telecom C-band when the waveguide cross-section approaches 5 μm^2.

The waveguide cross-section can be adjusted by gradually modifying the total thickness e_{LN}, the waveguide width, or the sidewall angle. In this study, we focus on the influence of membrane thickness on the conversion efficiency, as shown in Figure 4(b). The total thickness includes the etched rib height, fixed at 1.2 μm, while the width and sidewall angle are set at 3.8 μm and 16°, respectively. The study is conducted at fixed temperature to eliminate temperature-dependent birefringence effects. The conversion efficiency is given by[25,26]

$$\eta = \frac{P_{SH}}{P_{pump}^2 L^2} = \frac{8\pi^2}{\varepsilon_o c n_{pump}^2 n_{SH} \lambda_{pump}^2} \frac{OI^2 d_{31}^2}{A_{eff}} \text{sinc}^2\left(\frac{\Delta k L}{2}\right) \tag{3}$$

In this equation, P_{SH} and P_{pump} represent the output second-harmonic (SH) power and input pump power, respectively. c is the speed of light in vacuum, and ε_o is the vacuum permittivity. The second-order nonlinear coefficient d_{31} is set to 4.3 pm/V, and A_{eff} refers to the effective mode area. The spatial overlap integral between pump and SH modes is OI. The nonlinear interaction length, L, is set at 1 mm, corresponding to the membrane length. The phase mismatch Δk plays a crucial role in determining the efficiency and bandwidth of the frequency conversion. It is mainly influenced by the group velocity mismatch (GVM) between the pump and second-harmonic waves, as well as the group velocity dispersion (GVD). Among these, GVM has the most significant impact on the bandwidth: as GVM approaches zero, the phase matching condition becomes less sensitive to wavelength variations, resulting in a broader conversion bandwidth.

According to Figure 4(b), for thicknesses exceeding 1.87 μm, dual-phase matching is observed, allowing waveguide to operate at two distinct wavelengths. For instance, a 1.92 μm-thick waveguide supports phase matching at 1325 and 1620 nm, yielding SH wavelengths of 662 and 810 nm, respectively. By fine-tuning the thickness, the generated wavelength can be continuously controlled across this range. Notably, at a thickness of 1.86 μm, a broadband phase-matching response is achieved. Below this threshold, phase matching is no longer possible, underscoring a key limitation of LNOI technology, which is typically confined to submicron thicknesses. Regarding conversion efficiency, theoretical values reach

https://doi.org/10.1021/acsphotonics.5c01334
ACS Photonics XXXX, XXX, XXX−XXX

60%/W/cm^2 for wavelengths below 1500 nm and approximately 40%/W/cm^2 at longer wavelengths.

Experimental Validation. The rib waveguide is formed by etching the Ti-indiffused waveguide (see Supporting Information for more details), resulting in the following dimensions: a width of 3.83 μm, an etching depth of 1.23 μm, and a sidewall angle of 16°. The waveguide is subsequently thinned using the same membrane thinning process described previously, yielding a final membrane thickness of 1.96 μm. This structure was then characterized for SHG performance. Figure 5(a) presents the measured conversion efficiency as a function of waveguide thickness. Theoretical curves, corrected by considering the propagation losses in the nonlinear region, were incorporated alongside the measurements to validate the SHG behavior. These curves were obtained using a modified efficiency formula[27,28] derived from eq 3

$$\eta_{\text{corrected}} = \eta \times \exp\left(-\left(\alpha_{\text{pump}} + \frac{\alpha_{\text{SH}}}{2}\right)L_{\text{NL}}\right) \times \left[\frac{\sin^2\left(\frac{\Delta k L_{\text{NL}}}{2}\right) + \sinh^2\left(\frac{\left(\alpha_{\text{pump}} - \frac{\alpha_{\text{SH}}}{2}\right)L_{\text{NL}}}{2}\right)}{\left(\frac{\Delta k L_{\text{NL}}}{2}\right)^2 + \left(\frac{\left(\alpha_{\text{pump}} - \frac{\alpha_{\text{SH}}}{2}\right)L_{\text{NL}}}{2}\right)^2}\right] \quad (4)$$

where η represents the normalized conversion efficiency without considering losses, Δk is the wave-vector mismatch, and L_{NL} corresponds to the nonlinear interaction length, set to 1 mm in our case. The terms α_{pump} and α_{SH} denote the propagation losses of the pump and second harmonic signals, respectively, expressed in cm^{-1}.

The waveguide loss characterization was performed using the Fabry−Perot method.[29] The estimated total losses in the nonlinear region were 1.95 dB for the TE polarization and 0.61 dB for the TM polarization. These values remain relatively high compared to the average losses measured in a membrane without the rib waveguide. This is likely due to sidewall roughness, which is attributed to the quality of the etching mask. In the future, postprocessing techniques, such as annealing, will be considered to reduce these losses.

Nonlinear characterization was performed using two tunable external-cavity lasers (T100S-HP ES and CL), covering a wavelength range from 1350 to 1630 nm. The TM_{00} pump mode was coupled into the waveguide using a polarization-maintaining (PM) fiber, with precise alignment along the crystal's x-axis via a rotating stage. The SH output was collected using a high-NA microscope objective and measured with a silicon photodetector (Thorlabs S130C), while the pump power was recorded using a germanium photodetector (Thorlabs S132C).

To accurately determine the pump power at the nonlinear region input and the SH power at the output, we corrected the output powers by considering the average losses in the nonlinear section, the taper transition, Fresnel reflection, and microscope objective transmission. Figure 5(a) shows the conversion efficiency measured after four thinning steps, reducing the membrane thickness from 1.96 to 1.87 μm. The experimental results, supported by simulations, reveal the occurrence of dual phase-matching. These phase-matching points converge at a membrane thickness of 1.87 μm, where both the phase matching and GVM are equal to zero. Consequently, the waveguide with a 1.87 μm thickness exhibited a broadband response centered in the telecom window, covering ≈150 nm. This represents the widest spectral bandwidth ever recorded through dispersion engineering in the telecom range using $\chi^{(2)}$ process in $LiNbO_3$, while maintaining a competitive conversion efficiency of 35%/W/cm^2.

All measurements were performed at room temperature, demonstrating the robustness of the SHG process without requiring active temperature tuning. This contrasts with most frequency converters, which typically rely on temperature-controlled ovens to achieve phase matching.

Figure 5(a) highlights the precise thickness control achieved during fabrication, with a resolution of 20 nm. This control enables fine-tuning of the phase-matching wavelength with an accuracy of approximately 30 nm within the 1250−1650 nm range. Notably, this accuracy is sufficient when compared to the full-width at half-maximum (FWHM) of the spectral response, which varies between 40 and 150 nm in this spectral range. For comparison, this 150 nm bandwidth is approximately 15 times broader than that typically achieved with Type-0 QPM in standard PPLNOI waveguide.[4] As a result, thickness control of ±20 nm is sufficient to accurately tune the emission wavelength while maintaining efficient conversion.

Throughout the measurements, the waveguide exhibited excellent power handling, sustaining up to ≈1 W of input pump power without degradation (471 mW output pump power), corresponding to an SH output power of ≈180 μW (Figure 5(b)). No evidence of photorefractive effects was observed, neither for the high-power pump in the telecom range nor for the second-harmonic signal. The phase-matching response remained stable and reproducible across multiple wavelength sweeps (5 min each), further demonstrating the platform's reliability under experimental conditions.

Finally, Figure 5(b) illustrates the quadratic dependence of SH power on pump power at 1535 nm. Although this wavelength is not optimal for peak conversion efficiency, as it represents the lower limit of the erbium amplifier used, the results remain consistent with theoretical expectations. The membrane's high power tolerance confirms its suitability for nonlinear optical applications at high power levels, such as femtosecond laser frequency doubling. This demonstrates the potential of a single platform for dual-phase matching and broadband frequency conversion, without the need for temperature tuning.

■ CONCLUSIONS

In summary, the integration of precise thickness control in $LiNbO_3$ membranes between 400 nm and a few tens of microns has enabled the fabrication of high-performance photonic devices with significantly enhanced nonlinear conversion efficiency and bandwidth. The demonstrated SHG device, operating at a fixed temperature, exhibits a broad 150 nm bandwidth and a conversion efficiency of 35%/W/cm^2, showcasing the potential of our approach for various integrated photonics applications. For an interaction length of 1 cm and an input pump power of 1 W, the device can achieve an overall conversion efficiency of 35% while offering a broader spectral bandwidth of 150 nm. By combining the advantages of both thin-film and bulk photonic platforms, our method offers a versatile solution for efficient light injection and fabrication implementation. While demonstrated here on a poling-free component, the platform is fully compatible with periodic poling and can therefore accommodate quasi-phase-matched

https://doi.org/10.1021/acsphotonics.5c01334
ACS Photonics XXXX, XXX, XXX−XXX

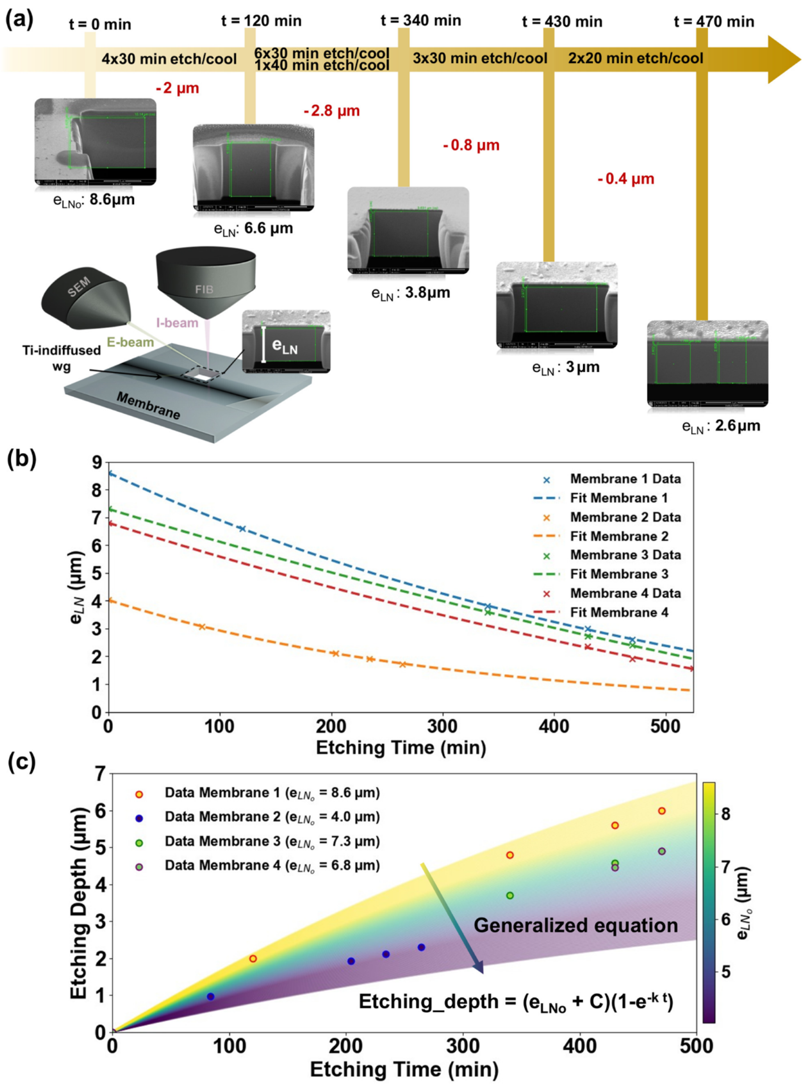

Figure 6. (a) Diagram showing SEM images of the membrane thickness evolution after each etching step. (b) Experimental plot of membrane thickness as a function of etching time for different initial thicknesses. The measurements follow the empirical calibration equation. (c) Evolution of etching depth versus etching time.

structures. Beyond making fabrication more accessible, the approach also offers postfabrication tunability through accurate membrane thickness control, positioning it as a promising technology for future applications in telecommunications, wavelength-division multiplexing, and quantum information processing.

■ METHODS

Precision Dicing for Local Waveguide Thinning. As previously described, the dicing process enables the membrane thickness to be reduced down to approximately 8 μm. However, achieving this target value requires an accurate measurement of the initial wafer thickness e before initiating the two thinning steps. A calibration procedure is first performed using the metallic blade on an unused region of the wafer. The blade is fully lowered, and the resulting groove footprint L is measured (see Figure 2(b)). Assuming a blade radius R = 50 mm, the wafer thickness e is then deduced from the geometric relation

$$e = R - \sqrt{R^2 - \left(\frac{L}{2}\right)^2} \qquad (5)$$

This method provides bulk thickness estimation with an accuracy of approximately 200 nm.

The same metallic blade used for calibration is subsequently employed to define the membrane cavity in five successive passes, resulting in a 500 μm wide groove and reducing the thickness to about 30 μm. The polishing blade is then employed to further reduce the membrane thickness to 8 μm while simultaneously improving the surface quality of the cavity sidewalls. As shown in Figure 2(b), the zoomed SEM image confirms the improved sidewall smoothness resulting from the polishing step. Once the membrane is formed, the bonded support wafer can either be removed to expose the freestanding region or retained to provide mechanical stability. The membrane thickness itself typically ranges from 7 to 9 μm. To further reduce the thickness and reach submicron values with nanometric precision, this process is then combined with a RIE post-thinning step. This RIE technique enables fine

https://doi.org/10.1021/acsphotonics.5c01334
ACS Photonics XXXX, XXX, XXX−XXX

control over the membrane thickness, achieving a precision of 20 nm.

Post-RIE Membrane Thickness Control. The post-thinning step is based on the empirical model described earlier in eq 1, which predicts the membrane thickness evolution as a function of etching time to achieve a targeted final thickness. This model was established from experimental data collected across multiple membranes, each with different initial thickness e_{LN_0} and etched for varying durations.

For each sample, a small window was opened in the membrane using a Focused Ion Beam (FIB), and the local thickness was measured using Scanning Electron Microscopy (SEM) (see Figure 6(a)). We show a progressive thinning of a membrane initially 8.60 μm thick, reduced to 2.60 μm after several RIE cycles. The resulting data points are plotted in blue in Figure 6(b). Additional measurements were conducted on other membranes with starting thicknesses of 7.30 μm, 6.80 μm, and 4.00 μm, which were thinned down to 2.10 μm, 1.57 μm, and 1.72 μm, respectively. These results are represented by the green, red, and orange curves in the same figure. All thickness evolutions were fitted using the relation 1.

Figure 6(c) further confirms the validity of this empirical model. It shows the etching depth as a function of etching time for membranes with initial thicknesses ranging from 2 to 10 μm. The etching rate, or the slope of the curve, varies with the membrane's initial thickness: thicker membranes exhibit higher etching rates. For instance, in the yellow region of the graph, corresponding to initial thicknesses between 8 and 10 μm, the etching rate remains high at approximately 17 nm/min. As the membrane becomes thinner, the etching rate gradually decreases, eventually leveling off to a horizontal asymptote. This phenomenon occurs earlier for membranes with smaller initial thicknesses, as seen in the blue section of Figure 6(c).

The variation in etching rates can primarily be attributed to the chemical reaction occurring during the etching process, which is related to the interaction of fluorine radicals with the $LiNbO_3$ surface. The foreseen etching reaction can be presented in the following form[30]

$$LiNbO_3 + F^* \rightarrow LiF \downarrow + NbF_x \uparrow + O_2 \uparrow + OF_2 \uparrow \quad (6)$$

This reaction produces several byproducts at the etched surface. The adsorption of these products is highly dependent on the surface temperature, leading to a temperature-dependent etching rate regime. The temperature gradient between the surface in contact with the plasma and the surface in contact with the thermalized shuttle plays a crucial role. For thicker membranes, the surface temperature is higher than the one at the bottom, which is fixed at 20 °C, influencing the etching process. This temperature difference leads to two distinct regimes: one with a high etching rate (around 17 nm/min), driven by the high surface temperature, which enables the evacuation of volatile byproducts, such as niobium pentafluoride (NbF_5), which desorbs at high temperatures (boiling point of NbF_5: 235 °C[31]). In contrast, lower etching rates occur when thermal equilibrium is reached between the etched surface and the shuttle, resulting in the accumulation of byproducts, such as NbF_5 or lithium fluoride (LiF),[30,32] on the surface. This accumulation, due to the temperature decrease, leads to a masking of the etched area, thereby reducing the effectiveness of mechanical etching by Ar ions. This behavior has been observed in other studies with thicker samples (e.g., 500 μm thick) operating in a high-temperature range of 80 to 300 °C.[30,33] This residual layer on the etched surface can lead to an increase of the optical propagation losses. To mitigate this issue and preserve low-loss optical performance, a post-etching cleaning step using a 2:1 solution of ammonia (NH_4OH) and hydrogen peroxide (H_2O_2) is applied. This treatment effectively eliminates surface byproducts and preserves the membrane's optical quality.

■ ASSOCIATED CONTENT

Supporting Information

The Supporting Information is available free of charge at https://pubs.acs.org/doi/10.1021/acsphotonics.5c01334.

Additional details on the fabrication process of the rib waveguide using RIE with a metallic hard mask, as well as the reflectometry method for nondestructive membrane thickness measurements, including an example of a thickness profile measured along the membrane (PDF)

■ AUTHOR INFORMATION

Corresponding Author

Nadège Courjal − *Université Marie et Louis Pasteur, CNRS, Institut FEMTO-ST, F- 25000 Besançon, France*; Email: nadege.courjal@femto-st.fr

Authors

Aiman Zinaoui − *Université Marie et Louis Pasteur, CNRS, Institut FEMTO-ST, F- 25000 Besançon, France*; orcid.org/0009-0000-5432-1983

Martin Khouri − *Université Marie et Louis Pasteur, CNRS, Institut FEMTO-ST, F- 25000 Besançon, France*

Jean-David Fayssaud − *Université Marie et Louis Pasteur, CNRS, Institut FEMTO-ST, F- 25000 Besançon, France*

Arthur De Sousa Lopes Moreira − *Université Marie et Louis Pasteur, CNRS, Institut FEMTO-ST, F- 25000 Besançon, France*

Miguel Angel Suarez − *Université Marie et Louis Pasteur, CNRS, Institut FEMTO-ST, F- 25000 Besançon, France*

Samuel Queste − *Université Marie et Louis Pasteur, CNRS, Institut FEMTO-ST, F- 25000 Besançon, France*

Laurent Robert − *Université Marie et Louis Pasteur, CNRS, Institut FEMTO-ST, F- 25000 Besançon, France*

Ludovic Gauthier-Manuel − *Université Marie et Louis Pasteur, CNRS, Institut FEMTO-ST, F- 25000 Besançon, France*

Mathieu Chauvet − *Université Marie et Louis Pasteur, CNRS, Institut FEMTO-ST, F- 25000 Besançon, France*; orcid.org/0000-0003-4158-1668

Complete contact information is available at: https://pubs.acs.org/10.1021/acsphotonics.5c01334

Notes

The authors declare no competing financial interest.

■ ACKNOWLEDGMENTS

This work has been partially funded by the SYRAH-lab project (contract "ANR-19- LCV2-0007-01") and the NanoFiLN project (ANR-23-PEEL-0004), supported by the EIPHI Graduate school (contract "ANR-17-EURE-0002"), the French RENATECH network through its FEMTO-ST technological facility, and the SMARTLIGHT platform funded by the Agence Nationale de la Recherche (EQUIPEX+

contract ≪ ANR-21-ESRE-0040 ≫) and Région Bourgogne Franche-Comté.

■ REFERENCES

(1) Boes, A.; Chang, L.; Langrock, C.; Yu, M.; Zhang, M.; Lin, Q.; Lončar, M.; Fejer, M.; Bowers, J.; Mitchell, A. Lithium niobate photonics: Unlocking the electromagnetic spectrum. *Science* **2023**, *379*, No. eabj4396, DOI: 10.1126/science.abj4396.

(2) Jia, Y.; Wang, L.; Chen, F. Ion-cut lithium niobate on insulator technology: Recent advances and perspectives. *Appl. Phys. Rev.* **2021**, *8*, No. 011307.

(3) Wang, X.; Jiao, X.; Wang, B.; Liu, Y.; Xie, X.-P.; Zheng, M.-Y.; Zhang, Q.; Pan, J.-W. Quantum frequency conversion and single-photon detection with lithium niobate nanophotonic chips. *npj Quantum Inf.* **2023**, *9*, No. 38.

(4) Wang, C.; Langrock, C.; Marandi, A.; Jankowski, M.; Zhang, M.; Desiatov, B.; Fejer, M. M.; Lončar, M. Ultrahigh-efficiency wavelength conversion in nanophotonic periodically poled lithium niobate waveguides. *Optica* **2018**, *5*, 1438−1441.

(5) He, J.; Chen, H.; Pan, K.; Su, Y.; Zhang, X.; Li, W.; Zhu, S.-N.; Hu, X. Heterogeneously Integrated Lithium Niobate on Insulator Chip for Frequency Up-Conversion and Detection. *ACS Photonics* **2024**, *11*, 4111−4115.

(6) Xie, Z.; Bo, F.; Lin, J.; Hu, H.; Cai, X.; Tian, X.-H.; Fang, Z.; Chen, J.; Wang, M.; Chen, F.; Cheng, Y.; Xu, J.; S Z. Recent development in integrated Lithium niobate photonics. *Adv. Phys.: X* **2024**, *9*, No. 2322739.

(7) Jankowski, M.; Mishra, J.; Fejer, M. M. Dispersion-engineered $\chi^{(2)}$ nanophotonics: a flexible tool for nonclassical light. *J. Phys.: Photonics* **2021**, *3*, No. 042005.

(8) Chen, M.; Wang, C.; Jia, K.; Tian, X.-H.; Tang, J.; Zhu, C.; Gu, X.; Zhao, Z.; Wang, Z.; Ye, Z.; Tang, J.; Zhang, Y.; Yan, Z.; Wang, X.; Qian, G.; Jin, B.; Wang, Z.; Zhu, S.-N.; Xie, Z. High-gain optical parametric amplification with a continuous-wave pump using a domain-engineered thin-film lithium niobate waveguide. *Optica* **2025**, *12*, 1242−1249.

(9) Chen, P.-K.; Briggs, I.; Cui, C.; Zhang, L.; Shah, M.; Fan, L. Adapted poling to break the nonlinear efficiency limit in nano-photonic lithium niobate waveguides. *Nat. Nanotechnol.* **2024**, *19*, 44−50.

(10) Assumpcao, D.; Renaud, D.; Baradari, A.; Zeng, B.; De-Eknamkul, C.; Xin, C. J.; Shams-Ansari, A.; Barton, D.; Machielse, B.; Loncar, M. A thin film lithium niobate near-infrared platform for multiplexing quantum nodes. *Nat. Commun.* **2024**, *15*, No. 10459.

(11) Jia, D.; Luo, Q.; Yang, C.; Ma, R.; Yu, X.; Gao, F.; Yang, Q.; Bo, F.; Zhang, G.; Xu, J. High-efficiency and easy-processing thin-film lithium niobate edge coupler. *Appl. Phys. Lett.* **2024**, *125*, No. 183503.

(12) Guo, Z.; Liu, W.; Wen, C.; Song, L.; Liu, L.; Dai, D.; Shi, Y. Polarization-insensitive and high-efficiency edge coupler for thin-film lithium niobate. *Opt. Lett.* **2024**, *49*, 2537−2540.

(13) Kuo, P. S. Noncritical phasematching behavior in thin-film lithium niobate frequency converters. *Opt. Lett.* **2022**, *47*, 54−57.

(14) Zhang, Y.; Li, H.; Ding, T.; Huang, Y.; Liang, L.; Sun, X.; Tang, Y.; Wang, J.; Liu, S.; Zheng, Y.; Chen, X. Scalable, fiber-compatible lithium-niobate-on-insulator micro-waveguides for efficient nonlinear photonics. *Optica* **2023**, *10*, 688−693.

(15) Lu, C.; Zhang, Y.; Qiu, J.; Tang, Y.; Ding, T.; Liu, S.; Zheng, Y.; Chen, X. Highly tunable birefringent phase-matched second-harmonic generation in an angle-cut lithium niobate-on-insulator ridge wave-guide. *Opt. Lett.* **2022**, *47*, 1081−1084.

(16) Courjal, N.; Caspar, A.; Calero, V.; Ulliac, G.; Suarez, M.; Guyot, C.; Bernal, M.-P. Simple production of membrane-based LiNbO3 micro-modulators with integrated tapers. *Opt. Lett.* **2016**, *41*, 5110−5113.

(17) Mwangi, M.; Behague, F.; Coste, A.; Safioui, J.; Suarez, M.; Byiringiro, J.; Lutz, P.; Clévy, C.; Courjal, N. In-situ phase control of a low-loss membrane-based lithiumniobate polarisation-state modulator. *Opt. Continuum* **2022**, *1*, 2513−2520.

(18) Zinaoui, A.; Grosjean, L.; De Sousa Lopes Moreira, A.; Suarez, M. A.; Queste, S.; Robert, L.; Gauthier-Manuel, L.; Chauvet, M.; Courjal, N. Broadband and widely tunable second harmonic generation in suspended thin-film LiNbO3 rib waveguides. *APL Photonics* **2024**, *9*, No. 101303.

(19) Hwang, A. Y.; Stokowski, H. S.; Park, T.; Jankowski, M.; McKenna, T. P.; Langrock, C.; Mishra, J.; Ansari, V.; Fejer, M. M.; Safavi-Naeini, A. H. Mid-infrared spectroscopy with a broadly tunable thin-film lithium niobate optical parametric oscillator. *Optica* **2023**, *10*, 1535−1542.

(20) Ludlow, A. D.; Boyd, M. M.; Ye, J.; Peik, E.; Schmidt, P. O. Optical atomic clocks. *Rev. Mod. Phys.* **2015**, *87*, 637−701.

(21) Jankowski, M.; Langrock, C.; Desiatov, B.; Marandi, A.; Wang, C.; Zhang, M.; Phillips, C. R.; Lončar, M.; Fejer, M. M. Ultrabroadband nonlinear optics in nanophotonic periodically poled lithium niobate waveguides. *Optica* **2020**, *7*, 40−46.

(22) Wu, X.; Zhang, L.; Hao, Z.; Zhang, R.; Ma, R.; Bo, F.; Zhang, G.; Xu, J. Broadband second-harmonic generation in step-chirped periodically poled lithium niobate waveguides. *Opt. Lett.* **2022**, *47*, 1574−1577.

(23) Jundt, D. H. Temperature-dependent Sellmeier equation for the index of refraction, n_e, in congruent lithium niobate. *Opt. Lett.* **1997**, *22*, 1553−1555.

(24) Schlarb, U.; Betzler, K. Refractive indices of lithium niobate as a function of temperature, wavelength, and composition: A generalized fit. *Phys. Rev. B* **1993**, *48*, No. 15613.

(25) Boyd, R. W. *Nonlinear Optical*; Academic Press, 2003.

(26) Luo, R.; He, Y.; Liang, H.; Li, M.; Lin, Q. Highly tunable efficient second-harmonic generation in a lithium niobate nano-photonic waveguide. *Optica* **2018**, *5*, 1006−1011.

(27) Weigel, P. O.; Mookherjea, S. Design of folded hybrid silicon carbide-lithium niobate waveguides for efficient second-harmonic generation. *J. Opt. Soc. Am. B* **2018**, *35*, 593−600.

(28) Sutherland, R. L. *Handbook of Nonlinear Optics*; CRC Press, 2003.

(29) Gerthoffer, A.; Guyot, C.; Qiu, W.; Ndao, A.; Bernal, M.-P.; Courjal, N. Strong reduction of propagation losses in LiNbO3 ridge waveguides. *Opt. Mater.* **2014**, *38*, 37−41.

(30) Osipov, A. A.; Osipov, A. A.; Iankevich, G. A.; Speshilova, A. B.; Shakhmin, A.; Berezenko, V. I.; Alexandrov, S. E. Deep Etching of $LiNbO_3$ Using Inductively Coupled Plasma in SF_6 -Based Gas Mixture. *J. Microelectromech. Syst.* **2021**, *30*, 90−95.

(31) Capelli, E.; Konings, R. Thermodynamic assessment of the niobium-fluorine system by coupling density functional theory and CALPHAD approach. *J. Fluorine Chem.* **2018**, *208*, 55−64.

(32) Shen, B.; Hu, D.; Dai, C.; Yu, X.; Tan, X.; Sun, J.; Jiang, J.; Jiang, A. Advanced Etching Techniques of LiNbO3 Nanodevices. *Nanomaterials* **2023**, *13*, No. 2789.

(33) Osipov, A. A.; Alexandrov, S. E.; Iankevich, G. A. The effect of a lithium niobate heating on the etching rate in SF_6 ICP plasma. *Mater. Res. Express* **2019**, *6*, No. 046306.